

NeurOp-Diff: Continuous Remote Sensing Image Super-Resolution via Neural Operator Diffusion

Zihao Xu^{1,2}, Yuzhi Tang^{1,2*}, Bowen Xu^{1,2}, Qingquan Li^{1,2}

¹Guangdong Laboratory of Artificial Intelligence and Digital Economy (SZ), China

² Shenzhen University, China

{xuzihao, tangyuzhi}@gml.ac.cn, {bowenxu, liqq}@szu.edu.cn

Abstract

Most publicly accessible remote sensing data suffer from low resolution, limiting their practical applications. To address this, we propose a diffusion model guided by neural operators (NO) for continuous remote sensing image super-resolution (NeurOp-Diff). Neural operators are used to learn resolution representations at arbitrary scales, encoding low-resolution (LR) images into high-dimensional features, which are then used as prior conditions to guide the diffusion model for denoising. This effectively addresses the artifacts and excessive smoothing issues present in existing super-resolution (SR) methods, enabling the generation of high-quality, continuous super-resolution images. Specifically, we adjust the super-resolution scale by a scaling factor s , allowing the model to adapt to different super-resolution magnifications. Furthermore, experiments on multiple datasets demonstrate the effectiveness of NeurOp-Diff. Our code is available at <https://github.com/zerono000/NeurOp-Diff>.

1. Introduction

Remote sensing super-resolution (RSSR) is a key technology in remote sensing image processing [54], aiming to restore low-resolution remote sensing (LRRS) images to high resolution remote sensing (HRRS) images, thus enhancing spatial details in remote sensing imagery [40]. Despite advances in remote sensing technology that have greatly improved the spatial resolution of modern satellites, challenges related to resolution limitations persist [1]. On the other hand, different application scenarios, such as urban planning and agricultural monitoring, have varying requirements for image details and coverage. Continuous super-resolution can dynamically adjust the magnification factor according to specific needs [5, 44], providing greater adaptability. Moreover, remote sensing data comes from di-

*Corresponding Author.

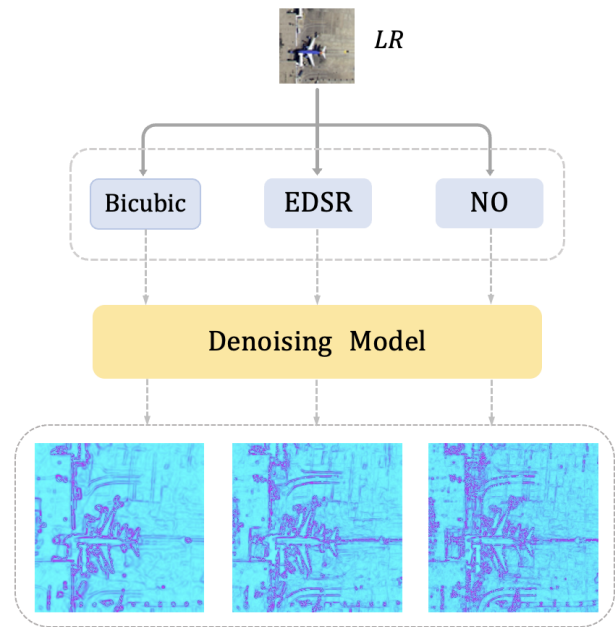


Figure 1. The figure illustrates the latent representations learned by the diffusion model after processing the low-resolution (LR) image using different methods, including Bicubic interpolation, EDSR, and Neural Operator (NO).

verse sources with varying resolutions. Continuous super-resolution helps integrate data of different resolutions, improving the efficiency and quality of data fusion.

Early regression-based methods performed image super-resolution by establishing a mapping between low-resolution (LR) and high-resolution (HR) images. These approaches often relied on deep convolutional neural networks (CNNs) [7, 8, 22, 30, 37, 50]. The advantages of these methods include stable training, simple and easy-to-optimize loss functions, typically using mean squared error (MSE) to minimize pixel-wise differences between

the reconstructed and ground-truth images. However, regression-based methods often result in overly smooth outputs that lack detail and struggle to recover realistic high-frequency information. On the other hand, variational autoencoders (VAEs) [23, 25] and generative adversarial networks (GANs) [9, 13, 20, 21, 27, 41] have demonstrated exceptional image generation capabilities. GANs, in particular, introduce an adversarial learning mechanism to produce more realistic high-resolution images. Compared to regression-based methods, GANs-based approaches better preserve image details, generating sharper and more natural results. However, the adversarial training process is unstable, requiring careful hyperparameter tuning and often encountering mode collapse issues. Moreover, GANs generated images may suffer from artifacts, leading to distortions in specific areas of the reconstructed images [13].

Recently, diffusion models (DMs) [16, 35] have gained attention for their strong performance in generating high-quality images. Compared to GANs, diffusion models exhibit greater stability during training and can generate more complex and realistic image structures. In the context of image super-resolution, methods like SR3 [34] iteratively refine high-resolution images by progressively denoising from noisy inputs, achieving excellent reconstruction results. However, such methods are constrained by fixed scaling factors [6, 17, 53], requiring separate models for different magnification scales, which increases computational cost. Furthermore, due to the limited integration of additional prior knowledge, their performance still has room for improvement.

In this paper, we propose the diffusion model using neural operators as conditional guidance (NeurOp-Diff), for continuous super-resolution of remote sensing images. By leveraging the neural operator’s ability to learn mappings between infinite-dimensional function spaces, we achieve continuous super-resolution for remote sensing images. The LRRS images processed by the neural operator serve as additional priors for the model’s denoising process. Unlike previous works that used bicubic upsampled LR images as prior knowledge, the neural operator dynamically updates latent bases through a multilayer Galerkin-type attention mechanism [44]. This process helps to recover certain high-frequency details, providing priors that enable the generation of more realistic high-resolution images [33] (see Figure 1). Experimental results demonstrate that the images generated by NeurOp-Diff surpass those produced by previous methods, both in quality and detail.

The contributions of this paper are summarized as follows:

- We propose a unified framework that integrates neural operators with diffusion models to remote sensing image super-resolution for the first time.
- We combined the high-frequency-rich continuous prior

with the diffusion model, enabling the reverse sampling process to better recover the detailed features and texture information from the original data.

- We conducted extensive experiments on three remote sensing datasets, and compared with five advanced methods, our results showed greater competitiveness.

2. Related Work

Remote Sensing Super-Resolution Generation Models.

Deep convolutional neural networks (CNNs) [7, 8, 22, 30, 37, 50] were among the earliest and most prominent methods for natural image super-resolution and have since been adapted to remote sensing image super-resolution (SR) due to their impressive performance. For example, LGCNet [46] uses a multi-branch structure to learn both local details and global environmental priors of remote sensing images, while RDBPN [51] employs a residual dense back-projection network to achieve large-scale super-resolution reconstruction. With the successful application of Transformers in computer vision [4, 11, 14, 31, 38, 43], Transformer-based super-resolution methods have started to gain significant attention. Although the SwinIR [29] model has shown excellent image reconstruction performance, it tends to struggle when it comes to restoring high-frequency details and complex textures. Simultaneously, GANs [9, 13, 20, 21, 27, 41] have shown strong potential for restoring image details. For example, EEGAN [19] employs a dense edge-enhancement network to reduce noise and improve edge contours. However, GANs are known for their unstable training process, which can lead to model collapse.

In recent years, denoising diffusion models (DDMs) [16, 35, 36] have emerged as a leading approach in the image generation domain. The denoising diffusion probabilistic model (DDPM) [16] introduced a new paradigm for image generation. Subsequent models such as Stable Diffusion [33] showcased the powerful capabilities of diffusion models in text-to-image generation, garnering significant attention. In specific tasks like image super-resolution, generative models have demonstrated unique advantages. For example, SR3 [34] achieves impressive super-resolution results by iterative refinement. However, its performance remains limited by insufficient prior knowledge. Recent works like Ref-Diff [10] and SGDM [39] incorporate semantic priors—land cover changes and vector maps—into conditional diffusion or generative models, enhancing fidelity and realism in large-scale remote sensing SR. However, they are still limited to fixed upscaling factors. To address this, we introduce neural operators based on SR3, enabling not only continuous super-resolution but also providing richer prior knowledge to enhance the denoising performance of the diffusion model.

Neural Operators. Neural operators are an emerging

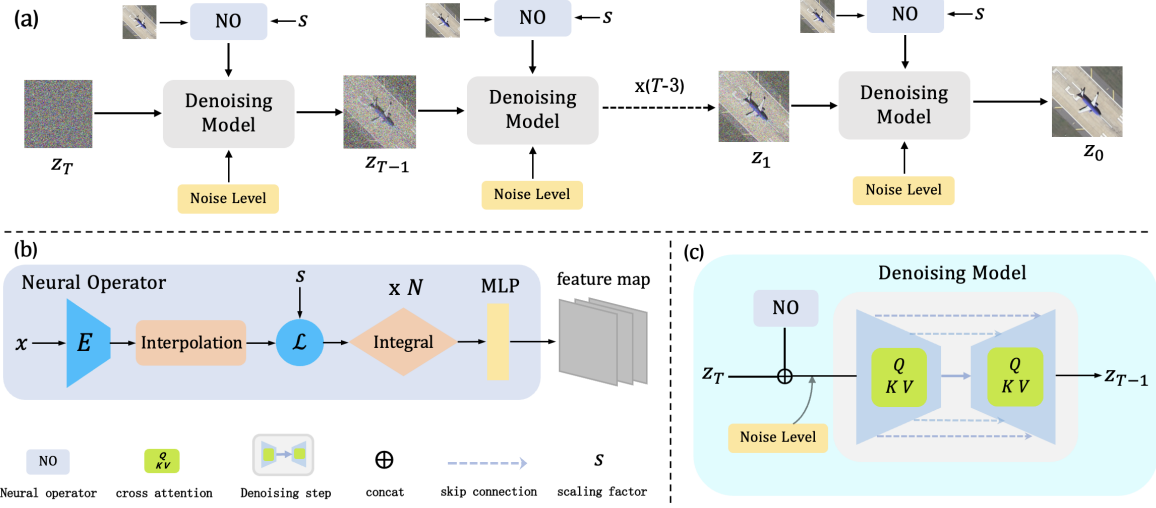


Figure 2. (a) The architecture of NeurOp-Diff. The noisy image is denoised through T iterations to generate a clear image. s is the scaling factor. (b) Neural operator architecture. The LR image is first encoded into high-dimensional features through the encoder (E), interpolation, and lifting functions (\mathcal{L}), which linearly transform low-resolution pixel values. Then, it passes through a kernel integral composed of Galerkin-type attention to produce the output features. Finally, MLP is applied for channel transformation. (c) The integration of neural operators and diffusion models. Here, Q , K , and V represent the components of the attention mechanism.

deep learning model capable of effectively learning and approximating complex nonlinear mappings while preserving the physical invariance and geometric structure of problems. This makes them particularly well-suited for solving complex partial differential equations [15, 18, 28, 32]. Unlike traditional neural networks, which typically learn mappings between finite-dimensional spaces, neural operators are designed to learn mappings from function space to function space, unconstrained by spatial dimensions. They can handle inputs of varying resolutions and sizes, producing corresponding functional outputs.

In recent years, neural operators have been applied to super-resolution tasks with promising results. For example, SRNO [44] employs a Galerkin-type attention mechanism and a multilayer architecture to treat the mapping from low-resolution to high-resolution images as a transformation in continuous function space, enabling fast, efficient, and dynamically adaptive super-resolution reconstruction. However, such methods often exhibit over-smoothing when restoring high-frequency details and textures in images. To address this, we integrate denoising diffusion models into our work. Diffusion models are capable of generating high-quality images with rich details and natural textures. By combining diffusion models with neural operators, our approach retains the advantage of neural operators in achieving continuous super-resolution while mitigating the issue of over-smoothing in image reconstruction.

3. Method

Given a set of remote sensing image datasets $D = \{(x^{(i)}, y^{(i)}, z^{(i)})\}_{i=1}^N$ and a control output resolution factor s , the datasets satisfy a specific joint probability distribution $p(X, Y, Z)$, where $x^{(i)}$ denotes the low-resolution source image, $y^{(i)}$ denotes the degraded high-resolution image obtained through the network, and $z^{(i)}$ denotes the ground-truth high-resolution image. Using the approximation of the conditional distribution $p(z|y)$ [45], we aim to map low-resolution images to their corresponding high-resolution counterparts.

NeurOp-Diff first initializes $z^{(i)}$ as pure noise $z_T^{(i)} \sim \mathcal{N}(0, I)$, and then refines it iteratively T times through the learned conditional transition distribution $p_\theta(z_{t-1}^{(i)} | z_t^{(i)}, y^{(i)})$ to generate high-resolution images $z_0^{(i)} \sim p(z | y)$. Here, θ denotes the learnable parameters of the neural network used to model the denoising process. The forward process defines how to progressively add noise to the initial $z_0^{(i)}$, generating the intermediate state sequence $(z_T^{(i)}, z_{T-1}^{(i)}, \dots, z_0^{(i)})$ via a fixed Markov transition probability $q(z_t | z_{t-1})$. Our goal is to reverse this diffusion process using the reverse chain based on $y^{(i)}$, achieving the task of recovering the signal from noisy data. The reverse chain employs a denoising model built upon a U-Net architecture, taking as input low-resolution images processed by neural operators and noisy target images. Details of the model are as follows (see Figure 2).

3.1. Conditional Denoising Diffusion Model

3.1.1. Forward Process

We first define a forward Markov diffusion process [16] q , which progressively adds noise to the initial image z_0 :

$$q(z_{1:T} | z_0) = \prod_{t=1}^T q(z_t | z_{t-1}). \quad (1)$$

The transition probability at each step is expressed as:

$$q(z_t | z_{t-1}) = \mathcal{N}(z_t; \sqrt{\alpha_t} z_{t-1}, (1 - \alpha_t)I), \quad (2)$$

where α_t is a hyperparameter controlling the noise level, satisfying $0 < \alpha_t < 1$. By marginalizing over intermediate steps, we can derive the boundary distribution of z_t given z_0 :

$$q(z_t | z_0) = \mathcal{N}(z_t; \sqrt{\gamma_t} z_0, (1 - \gamma_t)I), \quad (3)$$

where $\gamma_t = \prod_{i=1}^t \alpha_i$. Using the properties of Gaussian distributions, the posterior distribution $q(z_{t-1} | z_0, z_t)$ can be derived as [34]:

$$q(z_{t-1} | z_0, z_t) = \mathcal{N}(z_{t-1}; \mu, \sigma^2 I), \quad (4)$$

with:

$$\begin{aligned} \mu &= \frac{\sqrt{\gamma_{t-1}(1 - \alpha_t)}}{1 - \gamma_t} z_0 + \frac{\sqrt{\alpha_t}(1 - \gamma_{t-1})}{1 - \gamma_t} z_t, \\ \sigma^2 &= \frac{(1 - \gamma_{t-1})(1 - \alpha_t)}{1 - \gamma_t}. \end{aligned} \quad (5)$$

3.1.2. Reverse Process

The inference stage is a reverse Markov process, which is the opposite of the forward diffusion process. It starts from pure Gaussian noise z_T and progressively optimizes to generate z_0 . The process is defined as:

$$\begin{aligned} p_\theta(z_{0:T} | y) &= p(z_T) \prod_{t=1}^T p_\theta(z_{t-1} | z_t, y), \\ p(z_T) &= \mathcal{N}(z_T; 0, I), \\ p_\theta(z_{t-1} | z_t, y) &= \mathcal{N}(z_{t-1}; \mu_\theta(y, z_t, \gamma_t), \sigma_t^2 I). \end{aligned} \quad (6)$$

By learning the conditional distribution of the forward diffusion process $p_\theta(z_{t-1} | z_t, y)$, the inference process can approximate the true posterior distribution [35], the final optimization step of the model is [34]:

$$z_{t-1} = \frac{1}{\sqrt{\gamma_t}} \left(z_t - \frac{1 - \alpha_t}{\sqrt{1 - \gamma_t}} f_\theta(y, z_t, \gamma_t) \right) + \sqrt{1 - \alpha_t} \epsilon_t, \quad (7)$$

where $\epsilon_t \sim \mathcal{N}(0, I)$, and f_θ represents the noise prediction component.

3.2. Neural Operator

Neural operators map input functions to their latent representations and use kernel integration to capture global correlations in the function space. Specifically, we define a kernel function $K_t : \mathbb{R}^{d_r + d_r} \rightarrow \mathbb{R}^{d_r \times d_r}$, which operates on the hidden representations $\phi(\xi)$ and $\phi(\eta)$, rather than relying on spatial variables (ξ, η) [44]. Here, d_r denotes the feature dimension, and K_t represents the kernel generation function at the t -th layer. To efficiently explore the hidden representations $\phi(\xi)$, we will use multiple test functions to define these distributions, similar to single-head self-attention [26]. Let $\phi_i = \phi(\xi_i) \in \mathbb{R}^{d_r}$, for $i = 1, \dots, n_{h_f}$, where n_{h_f} denotes the number of pixels on the high-resolution grid.

The kernel integral operator $\mathcal{K}(\phi)$ can be approximated using Monte Carlo methods, as follows:

$$\begin{aligned} \mathcal{K}(\phi)(\xi) &= \int_{\Omega} K(\phi(\xi), \phi(\eta)) \phi(\eta) d\eta \\ &\approx \sum_{i=1}^{n_f} K(\phi(\xi), \phi_i) \phi_i, \quad \forall \xi \in \Omega_{h_f} \end{aligned} \quad (8)$$

where the kernel function $K(\phi(\xi), \phi_i)$ is computed as:

$$K(\phi(\xi), \phi_i) = \frac{\exp\left(\frac{\langle W_q \phi(\xi), W_k \phi_i \rangle}{\sqrt{d_r}}\right)}{\sum_{j=1}^{n_f} \exp\left(\frac{\langle W_q \phi_j, W_k \phi_i \rangle}{\sqrt{d_r}}\right)} W_v \quad (9)$$

Here, W_q , W_k , and W_v correspond to the query, key, and value matrices. Using this formulation, the kernel function can represent a combination of trainable functions.

The advantages of neural operators lie in their ability to handle data with different resolutions while capturing global relationships in the function space through inner product operations [44]. For example, a function f can be represented as a distribution function instead of being evaluated at individual coordinate points. We use query, key, and value functions $q(\xi)$, $k(\xi)$, and $v(\xi)$ to express global correlations, and the kernel integration operation can be represented as ($j = 1, \dots, d_r$):

$$((\mathcal{K}(\phi))(\xi))_j = \sum_{l=1}^{d_r} \langle k_l, v_j \rangle q_l(\xi), \quad \forall \xi \in \Omega_{h_f} \quad (10)$$

In the framework of neural operators, the latent representation ϕ is obtained through a linear combination of basis functions. To achieve efficient computation in high-resolution scenarios, Galerkin-type attention [3] is introduced. This mechanism achieves an approximately optimal solution through the linear combination of Q , K , and V :

$$\phi = Q(\tilde{K}^\top \tilde{V})/n_f, \quad (11)$$

where \tilde{K} and \tilde{V} are normalized keys and values. This method not only reduces computational complexity but also

effectively addresses discontinuities at feature boundaries. To further enhance expressive power, neural operators iteratively update representations through a feed-forward network (FFN $\mathcal{O} : \mathbb{R}^{d_r} \rightarrow \mathbb{R}^{d_r}$). The iterative process is described as:

$$\phi_{t+1}(\xi) = \phi_t(\xi) + \mathcal{O}((K_t(\phi_t))(\xi) + \phi_t(\xi)). \quad (12)$$

This iterative mechanism [44] enables neural operators to continuously enrich their representational capabilities, improving performance in ultra-high-resolution tasks.

3.3. Neural Operator with Conditional Diffusion

Although the Conditional Denoising Diffusion Model excels in high-fidelity reconstruction of target images, with strong denoising capabilities and high-quality generation performance, its input priors are typically derived from simple upsampling operations (e.g., bicubic interpolation), which have limited expressive power and are constrained by fixed scaling factors. In contrast, the Neural Operator can learn mappings between infinite-dimensional function spaces and extract latent continuous high-frequency information, effectively addressing the limitations of input prior expressiveness and fixed resolution. Therefore, we incorporate the Neural Operator into the Conditional Denoising Diffusion Model to enhance the expressive power of input priors, thereby improving the quality of generated images and enabling more flexible continuous super-resolution. Specifically, we first employ the Neural Operator \mathcal{F}_θ to process the low-resolution remote sensing image, obtaining a latent continuous prior representation:

$$y = \mathcal{F}_\theta(x), \quad (13)$$

where y encapsulates richer and more dynamic high-frequency information compared to traditional upsampling priors. Subsequently, during the reverse process of the diffusion model (as detailed in Equations (6) and (7)), this Neural Operator prior y is incorporated as conditional information into the noise prediction network \mathcal{G}_θ , thereby refining the sampling distribution at each diffusion inversion step.

In our model, given the intermediate state z_t in the diffusion process and the prior derived from the neural operator y , the reverse update equation is expressed as:

$$z_{t-1} = \frac{1}{\sqrt{\gamma_t}} \left(z_t - \frac{1 - \alpha_t}{\sqrt{1 - \gamma_t}} \mathcal{G}_\theta(y, z_t, \gamma_t) \right) + \sqrt{1 - \alpha_t} \epsilon_t \quad (14)$$

In this equation, $\mathcal{G}_\theta(y, z_t, \gamma_t)$ serves not only as the noise prediction component but also carries the latent function space prior provided by the Neural Operator. This integration allows for a more flexible and expressive guidance of the diffusion process updates. Through multi-layer

Galerkin-type attention mechanisms and dynamically updated latent bases, the neural operator captures complex features and high-frequency information at a global scale of the input image. When this information is incorporated as conditional guidance into the diffusion process, the model can progressively eliminate noise and converge toward more realistic and higher-resolution remote sensing image reconstructions during iterative sampling.

3.4. Network details

NeurOp-Diff network architecture is illustrated in the figure 2. The neural operator utilizes a scaling factor $s \sim \mathcal{U}(1, M)$ to ensure the model is effectively applicable to multiple scales. In this experiment, we set $M = 8$. For the feature encoder E , we reference the EDSR-baseline [30] by removing the last sampling layer. Regarding the noise level γ , we follow a uniform sampling method. First, the time step $t \sim \{0, T\}$ is sampled uniformly, followed by sampling γ from $\mathcal{U}(\gamma_{t-1}, \gamma_t)$. This process is expressed as: $\gamma \sim \frac{1}{T} \sum_{t=1}^T \mathcal{U}(\gamma_{t-1}, \gamma_t)$ [34].

4. Experiments

4.1. Training

Experimental Setup. In this experiment, we used three remote sensing datasets: UCMerced [48], AID [47] and RSSCN7 [55]. A portion of each dataset was used as the training set, while the remaining portion was used for evaluation. For AID [47] and RSSCN7 [55], which do not match the target resolution, we adjusted the data using center cropping [2] and downsampling. We compared NeurOp-Diff with various representative super-resolution methods, including both diffusion-based generative approaches and regression-based continuous super-resolution methods. To evaluate the effectiveness of our continuous super-resolution method, we also tested magnification factors beyond the training distribution when compared with SRNO [44]. During the training phase, the scaling factors were uniformly sampled within a continuous range from $\times 1$ to $\times 8$. In the testing phase, the model was further evaluated on images with out-of-distribution higher scaling factors, specifically from $\times 9$ to $\times 10$. The experimental results are primarily evaluated using PSNR (Peak Signal-to-Noise Ratio) and SSIM (Structural Similarity Index) [42].

Training Details. Following the referenced approach [44], we first pre-trained the neural operator component for 500 epochs with a batch size of 64. Then, we froze the weights of the neural operator and trained the entire NeurOp-Diff model. The batch size was set to 10, and approximately 1M iterations were performed. The Adam optimizer [24] was used, with an initial learning rate of 1×10^{-4} and a minimum learning rate of 2×10^{-6} . For the first 0.1

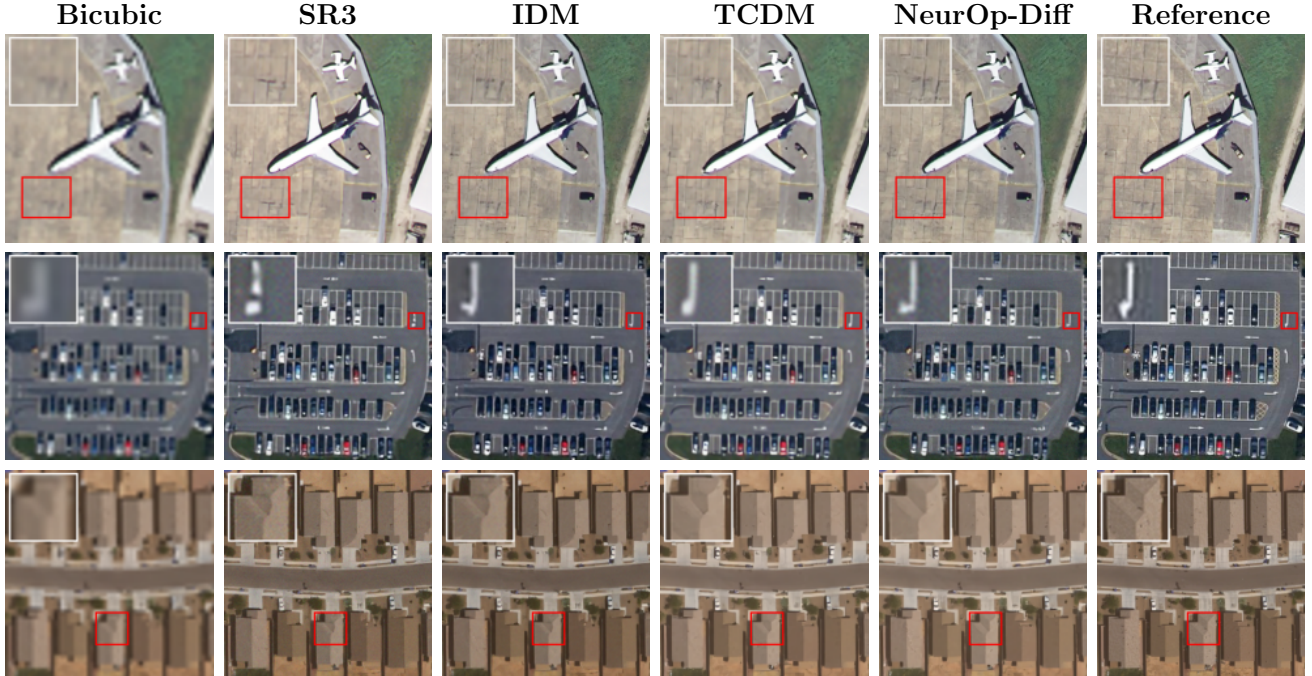


Figure 3. A visualization quality comparison between NeurOp-Diff and generative super-resolution (SR) models on UCMerced and AID. For each image, we also display finer details of the magnified regions.

M iterations, a constant learning rate was maintained, followed by a learning rate decay strategy. Dropout was set to 0.2 during training. During training, the scaling factor $s \sim \mathcal{U}(1, M)$ was sampled from a uniform distribution to cover multiple levels of magnification. For super-resolution tasks, a larger T generally yields better results. Therefore, in this experiment, we set $T = 2000$. And we chose the L_1 norm as the loss function. In the inference phase, we used a uniform sampling strategy [36] to accelerate inference. Experiments showed that setting the number of noise diffusion steps to 50 produced good inference results. The experiments were conducted on an NVIDIA RTX 4090 GPU.

4.2. Comparison of Generative SR

4.2.1. Qualitative Comparison

Figure 3 presents the super-resolution results of $64 \times 64 \rightarrow 256 \times 256$ for the UCMerced and AID remote sensing datasets. Compared with various state-of-the-art (SOTA) generative methods, NeurOp-Diff demonstrates excellent reconstruction capability. Although all methods can generally produce realistic super-resolution images, the magnified regions marked with rectangles reveal that NeurOp-Diff demonstrates superior reconstruction performance in recovering high-frequency components such as road textures and shadows, compared to other generative methods. This is attributed to the prior knowledge provided by the NO.

Dataset	Methods	x4		x8	
		PSNR	SSIM	PSNR	SSIM
UCMerced	SR3 [34]	27.15	0.7587	23.12	0.5846
	IDM [12]	27.66	0.7606	23.68	0.6131
	TCDM [52]	27.83	0.7679	24.17	0.6422
	NeurOp-Diff	28.14	0.7761	24.51	0.6502
AID	SR3 [34]	26.24	0.6709	22.54	0.5231
	IDM [12]	27.03	0.6778	22.90	0.5487
	TCDM [52]	27.53	0.6840	23.37	0.5584
	NeurOp-Diff	27.57	0.6845	23.45	0.5599
RSSCN7	SR3 [34]	26.22	0.5835	22.96	0.5329
	IDM [12]	27.18	0.6235	23.37	0.5603
	TCDM [52]	27.71	0.6489	23.69	0.5873
	NeurOp-Diff	27.74	0.6509	23.73	0.5889

Table 1. Quantitative comparison of various generative super-resolution ($64 \times 64 \rightarrow 256 \times 256$, $32 \times 32 \rightarrow 256 \times 256$) methods on UCMerced, AID, and RSSCN7 in terms of average PSNR and SSIM. The best performance are bolded.

4.2.2. Quantitative Comparison

Table 1 presents the PSNR and SSIM results of various models for 4x SR and 8x SR. Compared to other generative

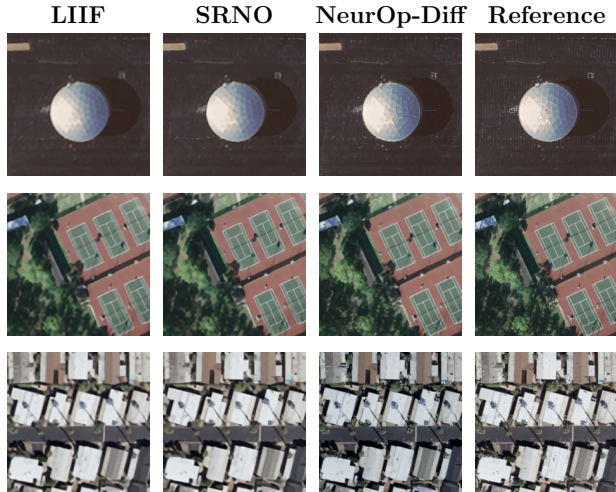


Figure 4. Qualitative comparison on 4x SR on UCMerced. Compared to regression-based methods, NeurOp-Diff is able to reconstruct more details and produce sharper textures.

models, NeurOp-Diff demonstrates superior performance in both pixel-level accuracy (PSNR) and visual perceptual quality (SSIM).

4.2.3. Runtime Efficiency Comparison

Table 2 shows a comparison of runtime between NeurOp-Diff and SR3, IDM under different inference steps. Although the runtime of all methods increases with the number of inference steps, our method maintains the fastest execution speed across all tested configurations.

Inference Steps	SR3 [34]	IDM [12]	NeurOp-Diff
T=30	1.8	1.47	1.12
T=50	2.16	1.79	1.52
T=100	3.23	2.87	2.61

Table 2. A comparison of the inference time (in seconds) required by different methods to process a single image under varying numbers of inference steps (T = 30, 50, 100).

4.3. Comparison of Continuous SR

Table 4 presents the quantitative comparison of LIIF, SRNO, and NeurOp-Diff on UCMerced. Although LIIF and SRNO achieve higher PSNR, our NeurOp-Diff demonstrates better performance in terms of SSIM. Moreover, in subjective perceptual differences (LPIPS) [49], the images generated by our model show smaller differences compared to the real images. As shown in Figure 4, regression-based continuous super-resolution methods struggle to reconstruct high-frequency details and restore realistic textures, often

producing overly smooth images. For instance, fine ground stripes are almost invisible in the images output by SRNO. Even when reconstructing more prominent stripes, the results appear somewhat blurry. In contrast, NeurOp-Diff demonstrates superior capability in restoring these details.

Furthermore, we randomly selected multiple magnification factors from the range (1, 8] and visualized images at these magnifications using both SRNO and NeurOp-Diff methods in Figure 5, in order to validate the performance of NeurOp-Diff in the continuous super-resolution task. Specifically, the real images were first downsampled according to the selected magnification factors to obtain corresponding low-resolution images. Then, SRNO and NeurOp-Diff were used to reconstruct these low-resolution images, generating high-resolution output images, such as 2x SR ($128 \times 128 \rightarrow 256 \times 256$), 4x SR ($64 \times 64 \rightarrow 256 \times 256$) and 8x SR ($32 \times 32 \rightarrow 256 \times 256$). During the reconstruction process, the output image resolution was fixed and unchanged.

From a quantitative perspective (see Table 3), although SRNO demonstrates slightly better PSNR values at lower magnification factors (e.g., 2x to 3.1x), NeurOp-Diff demonstrates superior performance in terms of SSIM metrics, which better aligns with human visual perception. As the magnification factor increases, the advantages of NeurOp-Diff become more apparent, particularly in challenging scenarios with higher magnification factors (e.g., 7x to 10x), where it consistently maintains higher SSIM values as well as lower LPIPS scores. Visually, NeurOp-Diff exhibits better performance in terms of the clarity of tennis court boundary lines and natural texture transitions in the surrounding environment. These advantages become more pronounced at higher magnification factors. This is primarily because NeurOp-Diff is better at capturing and reconstructing high-frequency information, allowing the generated images at high magnification factors to maintain high visual quality and detail richness. However, SRNO often struggles to fully recover complex texture details when handling larger magnifications, resulting in relatively lacking detail in the generated images.

4.4. Ablation Studies

To explore the impact of the LR conditional network, we conducted 4x super-resolution ablation experiments on remote sensing datasets. Specifically, we constructed comparison models by replacing the scale-adaptive conditional network in NeurOp-Diff with three different conditional mechanisms: (1) Concatenating the upsampled LR image directly with the ground truth image (SR3 [34]); (2) Concatenating LR features encoded by EDSR [30] with the ground truth image; (3) Concatenating LR features encoded by the neural operator with the ground truth image. As shown in Figure 1, directly using the upsampled LR image as a prior

Table 3. Quantitative comparison of continuous super-resolution (SR) results on UCMerced (PSNR/SSIM/LPIPS).

Method	Metric	in-distribution					out-of-distribution	
		2×	3.1×	5.8×	7×	8×	9×	10×
SRNO [44]	PSNR	34.32	31.05	27.19	25.73	24.67	24.32	23.92
	SSIM	0.786	0.746	0.681	0.649	0.623	0.607	0.592
	LPIPS	0.118	0.142	0.194	0.207	0.215	0.221	0.228
IDM [12]	PSNR	33.54	30.32	26.37	25.02	23.68	23.34	23.05
	SSIM	0.811	0.781	0.692	0.646	0.613	0.601	0.587
	LPIPS	0.103	0.119	0.187	0.208	0.219	0.225	0.230
NeurOp-Diff	PSNR	33.93	30.76	26.89	25.50	24.51	24.13	23.88
	SSIM	0.824	0.792	0.717	0.673	0.650	0.641	0.633
	LPIPS	0.098	0.112	0.159	0.188	0.195	0.206	0.212

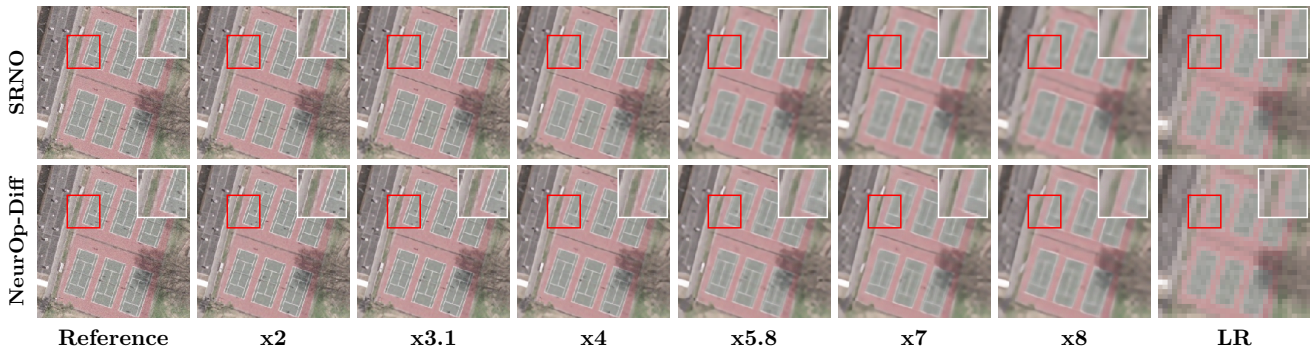


Figure 5. Visualization of continuous SR results on UCMerced. The resolution of the ground truth image is 256×256 . We randomly selected multiple magnification factors within the range of $(1, 8]$ for demonstration, additionally including two out-of-distribution magnification factors. (i.e., $5.8x$, $8x$, and $10x$).

Method	PSNR \uparrow	SSIM \uparrow	LPIPS \downarrow
LIIF [5]	28.96	0.69	0.182
SRNO [44]	29.21	0.72	0.164
NeurOp-Diff	28.14	0.78	0.136

Table 4. Quantitative comparison of NeurOp-Diff and regression methods for $4x$ SR on UCMerced.

condition results in the least amount of detail recovery. Encoding LR features with EDSR recovers more details, but it still falls short compared to the scale-adaptive network encoded by the neural operator. The quantitative results in Table 5 further validate the effectiveness of the neural operator-based conditioning mechanism, as it achieves the best performance in both PSNR and SSIM. In comparison, it is evident that LR images encoded by the neural operator provide more prior knowledge.

	Bicubic	EDSR	Neural Operator
PSNR \uparrow	27.15	27.42	28.14
SSIM \uparrow	0.7587	0.7602	0.7761

Table 5. Comparison of different methods by PSNR and SSIM

5. Conclusion

This paper presented Continuous Remote Sensing Image Super-Resolution via Neural Operator Diffusion (NeurOp-Diff). The method uses the LR remote sensing image encoded by the neural operator as the prior condition for the denoising process of the diffusion model, and achieves continuous super-resolution through the neural operator’s ability to map to infinite-dimensional function spaces. Experiments show that, compared to various advanced methods, our approach achieves superior results.

Acknowledgements

This work was supported by the National Natural Science Foundation of China (No. 42306245), in part by the National Key Research and Development Program of China (No. 2024YFF0617900), in part by the Shenzhen Outstanding Talents Training Fund, in part by the Shenzhen Major Science and Technology Project (No. KCXFZ20240903093000002), and in part by the Open Research Fund Program of MNR Key Laboratory for Geo-Environmental Monitoring of Great Bay Area (No. GEMLab-2023015).

References

- [1] Syed Muhammad Arsalan Bashir, Yi Wang, Mahrukh Khan, and Yilong Niu. A comprehensive review of deep learning-based single image super-resolution. *PeerJ Computer Science*, 7:e621, 2021. 1
- [2] Andrew Brock. Large scale gan training for high fidelity natural image synthesis. *arXiv preprint arXiv:1809.11096*, 2018. 5
- [3] Shuhao Cao. Choose a transformer: Fourier or galerkin. *Advances in neural information processing systems*, 34:24924–24940, 2021. 4
- [4] Hanting Chen, Yunhe Wang, Tianyu Guo, Chang Xu, Yiping Deng, Zhenhua Liu, Siwei Ma, Chunjing Xu, Chao Xu, and Wen Gao. Pre-trained image processing transformer. In *Proceedings of the IEEE/CVF conference on computer vision and pattern recognition*, pages 12299–12310, 2021. 2
- [5] Yinbo Chen, Sifei Liu, and Xiaolong Wang. Learning continuous image representation with local implicit function. In *Proceedings of the IEEE/CVF conference on computer vision and pattern recognition*, pages 8628–8638, 2021. 1, 8
- [6] Tao Dai, Jianrui Cai, Yongbing Zhang, Shu-Tao Xia, and Lei Zhang. Second-order attention network for single image super-resolution. In *Proceedings of the IEEE/CVF conference on computer vision and pattern recognition*, pages 11065–11074, 2019. 2
- [7] C. Dong, C. C. Loy, K. He, and X. Tang. Image super-resolution using deep convolutional networks. In *Proceedings of the IEEE Conference on Computer Vision and Pattern Recognition*, pages 184–192, 2015. 1, 2
- [8] C. Dong, C. C. Loy, and X. Tang. Accelerating the super-resolution convolutional neural network. In *Proceedings of the European Conference on Computer Vision*, pages 391–407, 2016. 1, 2
- [9] Runmin Dong, Lixian Zhang, and Haohuan Fu. Rrsgan: Reference-based super-resolution for remote sensing image. *IEEE Transactions on Geoscience and Remote Sensing*, 60: 1–17, 2021. 2
- [10] Runmin Dong, Shuai Yuan, Bin Luo, Mengxuan Chen, Jinxiao Zhang, Lixian Zhang, Weijia Li, Juepeng Zheng, and Haohuan Fu. Building bridges across spatial and temporal resolutions: Reference-based super-resolution via change priors and conditional diffusion model. In *Proceedings of the IEEE/CVF Conference on Computer Vision and Pattern Recognition*, pages 27684–27694, 2024. 2
- [11] Alexey Dosovitskiy. An image is worth 16x16 words: Transformers for image recognition at scale. *arXiv preprint arXiv:2010.11929*, 2020. 2
- [12] Sicheng Gao, Xuhui Liu, Bohan Zeng, Sheng Xu, Yanjing Li, Xiaoyan Luo, Jianzhuang Liu, Xiantong Zhen, and Baochang Zhang. Implicit diffusion models for continuous super-resolution. In *Proceedings of the IEEE/CVF conference on computer vision and pattern recognition*, pages 10021–10030, 2023. 6, 7, 8
- [13] Ian Goodfellow, Jean Pouget-Abadie, Mehdi Mirza, Bing Xu, David Warde-Farley, Sherjil Ozair, Aaron Courville, and Yoshua Bengio. Generative adversarial nets. *Advances in neural information processing systems*, 27, 2014. 2
- [14] Chun-Le Guo, Qixin Yan, Saeed Anwar, Runmin Cong, Wenqi Ren, and Chongyi Li. Image dehazing transformer with transmission-aware 3d position embedding. In *Proceedings of the IEEE/CVF conference on computer vision and pattern recognition*, pages 5812–5820, 2022. 2
- [15] Gaurav Gupta, Xiongye Xiao, and Paul Bogdan. Multiwavelet-based operator learning for differential equations. In *Advances in Neural Information Processing Systems*, pages 24048–24062, 2021. 3
- [16] Jonathan Ho, Ajay Jain, and Pieter Abbeel. Denoising diffusion probabilistic models. *Advances in neural information processing systems*, 33:6840–6851, 2020. 2, 4
- [17] Chih-Chung Hsu, Chia-Ming Lee, and Yi-Shiuan Chou. Drct: Saving image super-resolution away from information bottleneck. *arXiv preprint arXiv:2404.00722*, 2024. 2
- [18] Rakhon Hwang, Jae Yong Lee, Jin Young Shin, and Hyung Ju Hwang. Solving pde-constrained control problems using operator learning. In *Proceedings of the AAAI Conference on Artificial Intelligence*, pages 4504–4512, 2022. 3
- [19] Kui Jiang, Zhongyuan Wang, Peng Yi, Guangcheng Wang, Tao Lu, and Junjun Jiang. Edge-enhanced gan for remote sensing image superresolution. *IEEE Transactions on Geoscience and Remote Sensing*, 57(8):5799–5812, 2019. 2
- [20] Tero Karras, Timo Aila, Samuli Laine, and Jaakko Lehtinen. Progressive growing of gans for improved quality, stability, and variation. In *Proceedings of the International Conference on Learning Representations*, 2018. 2
- [21] Tero Karras, Samuli Laine, and Timo Aila. A style-based generator architecture for generative adversarial networks. In *Proceedings of the IEEE/CVF conference on computer vision and pattern recognition*, pages 4401–4410, 2019. 2
- [22] J. Kim, J. K. Lee, and K. M. Lee. Deeply-recursive convolutional network for image super-resolution. In *Proceedings of the IEEE Conference on Computer Vision and Pattern Recognition*, pages 1637–1645, 2016. 1, 2
- [23] J. Kim, J. K. Lee, and K. M. Lee. Accurate image super-resolution using very deep convolutional networks. In *Proceedings of the IEEE Conference on Computer Vision and Pattern Recognition*, pages 1646–1654, 2016. 2
- [24] Diederik P Kingma. Adam: A method for stochastic optimization. *arXiv preprint arXiv:1412.6980*, 2014. 5

- [25] Diederik P. Kingma and Max Welling. Auto-encoding variational bayes. In *Proceedings of the International Conference on Learning Representations*, 2013. 2
- [26] Nikola Kovachki, Zongyi Li, Burigede Liu, Kamyar Azizzadenesheli, Kaushik Bhattacharya, Andrew Stuart, and Anima Anandkumar. Neural operator: Learning maps between function spaces. *arXiv preprint arXiv:2108.08481*, 2021. 4
- [27] Christian Ledig, Lucas Theis, Ferenc Huszár, Jose Caballero, Andrew Cunningham, Alejandro Acosta, Andrew Aitken, Alykhan Tejani, Johannes Totz, Zehan Wang, et al. Photo-realistic single image super-resolution using a generative adversarial network. In *Proceedings of the IEEE conference on computer vision and pattern recognition*, pages 4681–4690, 2017. 2
- [28] Zongyi Li, Nikola Kovachki, Kamyar Azizzadenesheli, Burigede Liu, Kaushik Bhattacharya, Andrew Stuart, and Anima Anandkumar. Fourier neural operator for parametric partial differential equations. *arXiv preprint arXiv:2010.08895*, 2020. 3
- [29] Jingyun Liang, Jiezhong Cao, Guolei Sun, Kai Zhang, Luc Van Gool, and Radu Timofte. Swinir: Image restoration using swin transformer. In *Proceedings of the IEEE/CVF international conference on computer vision*, pages 1833–1844, 2021. 2
- [30] B. Lim, S. Son, H. Kim, S. Nah, and K. M. Lee. Enhanced deep residual networks for single image super-resolution. In *Proceedings of the IEEE Conference on Computer Vision and Pattern Recognition Workshops*, pages 136–144, 2017. 1, 2, 5, 7
- [31] Ze Liu, Yutong Lin, Yue Cao, Han Hu, Yixuan Wei, Zheng Zhang, Stephen Lin, and Baining Guo. Swin transformer: Hierarchical vision transformer using shifted windows. In *Proceedings of the IEEE/CVF international conference on computer vision*, pages 10012–10022, 2021. 2
- [32] Lu Lu, Pengzhan Jin, Guofei Pang, Zhongqiang Zhang, and George Em Karniadakis. Learning nonlinear operators via deepoNet based on the universal approximation theorem of operators. *Nature Machine Intelligence*, 3(3):218–229, 2021. 3
- [33] Robin Rombach, Andreas Blattmann, Dominik Lorenz, Patrick Esser, and Björn Ommer. High-resolution image synthesis with latent diffusion models. In *Proceedings of the IEEE/CVF conference on computer vision and pattern recognition*, pages 10684–10695, 2022. 2
- [34] Chitwan Saharia, Jonathan Ho, William Chan, Tim Salimans, David J Fleet, and Mohammad Norouzi. Image super-resolution via iterative refinement. *IEEE transactions on pattern analysis and machine intelligence*, 45(4):4713–4726, 2022. 2, 4, 5, 6, 7
- [35] Jascha Sohl-Dickstein, Eric Weiss, Niru Maheswaranathan, and Surya Ganguli. Deep unsupervised learning using nonequilibrium thermodynamics. In *International conference on machine learning*, pages 2256–2265, 2015. 2, 4
- [36] Jiaming Song, Chenlin Meng, and Stefano Ermon. Denoising diffusion implicit models. *arXiv preprint arXiv:2010.02502*, 2020. 2, 6
- [37] Arash Vahdat and Jan Kautz. Nvae: A deep hierarchical variational autoencoder. *Advances in neural information processing systems*, 33:19667–19679, 2020. 1, 2
- [38] A Vaswani. Attention is all you need. *Advances in Neural Information Processing Systems*, 2017. 2
- [39] Ce Wang and Wanjie Sun. Semantic guided large scale factor remote sensing image super-resolution with generative diffusion prior. *ISPRS Journal of Photogrammetry and Remote Sensing*, 220:125–138, 2025. 2
- [40] Peijuan Wang, Bulent Bayram, and Elif Sertel. A comprehensive review on deep learning based remote sensing image super-resolution methods. *Earth-Science Reviews*, 232: 104110, 2022. 1
- [41] Xintao Wang, Ke Yu, Shixiang Wu, Jinjin Gu, Yihao Liu, Chao Dong, Yu Qiao, and Chen Change Loy. Esrgan: Enhanced super-resolution generative adversarial networks. In *Proceedings of the European conference on computer vision (ECCV) workshops*, pages 0–0, 2018. 2
- [42] Zhou Wang, Alan C Bovik, Hamid R Sheikh, and Eero P Simoncelli. Image quality assessment: from error visibility to structural similarity. *IEEE transactions on image processing*, 13(4):600–612, 2004. 5
- [43] Zhendong Wang, Xiaodong Cun, Jianmin Bao, Wengang Zhou, Jianzhuang Liu, and Houqiang Li. Uformer: A general u-shaped transformer for image restoration. In *Proceedings of the IEEE/CVF conference on computer vision and pattern recognition*, pages 17683–17693, 2022. 2
- [44] Min Wei and Xuesong Zhang. Super-resolution neural operator. In *Proceedings of the IEEE/CVF Conference on Computer Vision and Pattern Recognition*, pages 18247–18256, 2023. 1, 2, 3, 4, 5, 8
- [45] Chanyue Wu, Dong Wang, Yunpeng Bai, Hanyu Mao, Ying Li, and Qiang Shen. Hsr-diff: Hyperspectral image super-resolution via conditional diffusion models. In *Proceedings of the IEEE/CVF International Conference on Computer Vision*, pages 7083–7093, 2023. 3
- [46] Tzu-Han Wu and Kuan-Wen Chen. Lgcnet: Feature enhancement and consistency learning based on local and global coherence network for correspondence selection. In *2023 IEEE International Conference on Robotics and Automation*, pages 6182–6188, 2023. 2
- [47] Gui-Song Xia, Jingwen Hu, Fan Hu, Baoguang Shi, Xiang Bai, Yanfei Zhong, Liangpei Zhang, and Xiaoqiang Lu. Aid: A benchmark data set for performance evaluation of aerial scene classification. *IEEE Transactions on Geoscience and Remote Sensing*, 55(7):3965–3981, 2017. 5
- [48] Yi Yang and Shawn Newsam. Bag-of-visual-words and spatial extensions for land-use classification. In *Proceedings of the 18th SIGSPATIAL international conference on advances in geographic information systems*, pages 270–279, 2010. 5
- [49] Richard Zhang, Phillip Isola, Alexei A Efros, Eli Shechtman, and Oliver Wang. The unreasonable effectiveness of deep features as a perceptual metric. In *Proceedings of the IEEE conference on computer vision and pattern recognition*, pages 586–595, 2018. 7
- [50] Y. Zhang, Y. Tian, Y. Kong, B. Zhong, and Y. Fu. Residual dense network for image super-resolution. In *Proceed-*

ings of the IEEE Conference on Computer Vision and Pattern Recognition, pages 2472–2481, 2018. [1](#), [2](#)

- [51] Yulun Zhang, Yapeng Tian, Yu Kong, Bineng Zhong, and Yun Fu. Residual dense network for image super-resolution. In *Proceedings of the IEEE conference on computer vision and pattern recognition*, pages 2472–2481, 2018. [2](#)
- [52] Yan Zhang, Hanqi Liu, Zhenghao Li, Xinbo Gao, Guangyao Shi, and Jianan Jiang. Tcdm: Effective large-factor image super-resolution via texture consistency diffusion. *IEEE Transactions on Geoscience and Remote Sensing*, 62:1–13, 2024. [6](#)
- [53] Hongyang Zhou, Xiaobin Zhu, Jianqing Zhu, Zheng Han, Shi-Xue Zhang, Jingyan Qin, and Xu-Cheng Yin. Learning correction filter via degradation-adaptive regression for blind single image super-resolution. In *Proceedings of the IEEE/CVF International Conference on Computer Vision*, pages 12365–12375, 2023. [2](#)
- [54] Xiao Xiang Zhu, Devis Tuia, Lichao Mou, Gui-Song Xia, Liangpei Zhang, Feng Xu, and Friedrich Fraundorfer. Deep learning in remote sensing: A comprehensive review and list of resources. *IEEE geoscience and remote sensing magazine*, 5(4):8–36, 2017. [1](#)
- [55] Qin Zou, Lihao Ni, Tong Zhang, and Qian Wang. Deep learning based feature selection for remote sensing scene classification. *IEEE Geoscience and Remote Sensing Letters*, 12(11):2321–2325, 2015. [5](#)